International Journal of Plasticity 150 (2022) 103193

Contents lists available at ScienceDirect

International Journal of Plasticity

journal homepage: www.elsevier.com/locate/ijplas

Effect of nickel addition on enhancing nano-structuring and suppressing TRIP effect in $Fe_{40}Mn_{40}Co_{10}Cr_{10}$ high entropy alloy during high-pressure torsion

Avanish Kumar Chandan [a,b,*], Kaushal Kishore [a,c], Pham Tran Hung [d], Mainak Ghosh [a,b], Sandip Ghosh Chowdhury [a,b], Megumi Kawasaki [e], Jenő Gubicza [d,*]

[a] Academy of Scientific and Innovative Research (AcSIR), Ghaziabad, 201002, India
[b] Materials Engineering Division, CSIR-National Metallurgical Laboratory, P.O.: Burmamines, Jamshedpur 831007, India
[c] Research & Development and Scientific Services, Tata Steel Limited, Jamshedpur, 831007, India
[d] Department of Materials Physics, Eötvös Loránd University, P.O.B. 32, Budapest H-1518, Hungary
[e] School of Mechanical, Industrial and Manufacturing Engineering, Oregon State University, Corvallis, OR 97331, United States

ARTICLE INFO

Keywords:
Dislocations (A)
Microstructures (A)
Phase transformation (A)
Strengthening mechanisms (A)
Twinning (A)

ABSTRACT

The present work unravels the effect of nickel (Ni) addition on the deformation mechanism and hardness evolution in a $Fe_{40}Mn_{40}Co_{10}Cr_{10}$ high entropy alloy (HEA) during high-pressure torsion (HPT) processing. For this purpose, two variants of the high entropy Cantor alloy, with compositions (atomic%) $Fe_{40}Mn_{40}Co_{10}Cr_{10}$ (Ni0 alloy) and $Fe_{35}Mn_{35}Co_{10}Cr_{10}Ni_{10}$ (Ni10 alloy) were selected. The study revealed a transition in the predominant plasticity mechanism with addition of Ni from TRIP in Ni0 to dislocation slip in Ni10 alloy. Such transition of plasticity mechanism was the direct consequence of an increase in the free energy of phase transformation, $\Delta G^{\gamma\rightarrow\varepsilon}$ towards a more positive value with Ni addition. Interestingly, the Ni10 alloy showed a greater extent of nano-structuring than the Ni0 alloy with nearly three-fold refined grain sizes, that is, lesser than 30 nm in Ni10 alloy and ~90 nm in Ni0 alloy. Furthermore, a 3–4 times higher dislocation density was observed in the FCC phase of the Ni10 alloy compared to that in the transformed HCP phase in the Ni0 alloy for any given HPT processing conditions. These differences in mechanism(s) of deformation and the extent of nano-structuring manifested as a greater ability of Ni added Ni10 alloy to harden itself during HPT. The present study suggests that a large fraction of hard HCP phase originating from TRIP effect in the Ni0 alloy has a lower hardening ability than the high dislocation density and nano-structuring in the Ni10 alloy.

1. Introduction

High entropy alloy (HEA) is a novel class of metallic alloys in which there is no principal element; instead these alloys consist of five or more elements in the range of 5–35 atomic% each (Cantor et al., 2004; Yeh et al., 2004). The underlying concept of HEA has opened up enormous possibilities in alloy development and subsequently the likelihood of discovering new alloy chemistries with superior

* Corresponding authors.
E-mail addresses: avanish@nmlindia.org (A.K. Chandan), jeno.gubicza@ttk.elte.hu (J. Gubicza).

https://doi.org/10.1016/j.ijplas.2021.103193
Received 20 October 2021; Received in revised form 25 December 2021;
Available online 27 December 2021

properties increased by many-folds (Miracle and Senkov, 2017; Srivastan and Gupta, 2020). A large number of HEAs pertaining to different classes have performed extraordinarily in a multitude of anticipated applications and highlighted the prowess of HEAs in development of materials with exotic properties. For instance, HEAs have shown to overcome the strength-ductility trade-off at various temperatures (Ding et al., 2018; Gludovatz et al., 2014; Li et al., 2016b; Ming et al., 2019; Nene et al., 2018; Zhang et al., 2020b) and to possess exceptional damage tolerance properties (Gludovatz et al., 2014, 2016; Thapliyal et al., 2020), superplastic behavior (Nene et al., 2020; Nguyen et al., 2020; Reddy et al., 2017), excellent corrosion resistance (Nene et al., 2019; Thapliyal et al., 2020), adequate fatigue resistance (Liu et al., 2019a) etc.

In the HEAs developed so far, Cantor alloy, i.e. the equiatomic FeMnCoCrNi alloy (Cantor et al., 2004) has received significantly high attention from research community owing to its intriguing ability to stabilize a single phase face-centered cubic (FCC) structure and an outstanding cryogenic damage tolerance properties (Gludovatz et al., 2014). This particular alloy exhibited a superior combination of strength (>1250 MPa) and ductility (> 75%) along with an exceptional fracture toughness value >200 MPa.m$^{1/2}$ at 77 K (Gludovatz et al., 2014). Considering the HEA compositions with even better mechanical properties, the definition of HEA was relaxed with the span of time. This triggered a large-scale exploration of compositional derivatives of the Cantor alloy. A variety of the Cantor alloy's derivatives also showed remarkable mechanical properties, especially at room temperature and sub-zero temperatures (Wung et al., 2018; Gludovatz et al., 2016; He et al., 2019; Li et al., 2016b; Miao et al., 2017; Tong et al., 2019). Akin to the Cantor alloy, its derivatives also stabilize an FCC crystal structure. However, contrary to the excellent mechanical properties at subzero temperatures, in general, this class of HEAs did not show remarkable mechanical properties at room temperature (RT). Although an FCC crystal structure ensures a decent tensile ductility, the low strength levels obtained at RT remained a setback. In order to overcome this limitation and to achieve superior strengths at ambient temperature, researchers resorted to the conventional strengthening mechanisms namely grain-refinement (Asghari-rad et al., 2019; He et al., 2019; Li et al., 2016a; Schneider et al., 2020), precipitation hardening (Li et al., 2020; Ming et al., 2018), transformation strengthening (He et al., 2019; Li et al., 2016b; Sinha et al., 2019), Taylor hardening (Gubicza et al., 2019b; Heczel et al., 2017) etc. To this end, a decrease in grain size can effectively strengthen the material, commonly also known as Hall-Petch strengthening. In FCC alloys, the severe plastic deformation (SPD) route including high-pressure torsion (HPT), equal-channel angular pressing (ECAP), accumulative roll bonding (ARB) etc., provides a superior option than the conventional thermomechanical processing route for obtaining ultrafine or even nano-structured materials that can demonstrate unprecedented strength levels (Valiev et al., 2000). Research in the effect of various SPD processing on the microstructural evolution and mechanical properties of the FCC HEAs has been carried out extensively (Gubicza et al., 2019b; Praveen et al., 2018b; Shahmir et al., 2017; Wang et al., 2021). Among the SPD techniques, HPT is considered as one of the most promising processing techniques for achieving significant grain refinement (Zhilyaev and Langdon, 2008). Cantor alloy and its derivatives processed by HPT under the different processing conditions showed the formation of nano-structured microstructures (Chandan et al., 2021a; Gubicza et al., 2019b; Heczel et al., 2017; Schuh et al., 2015). Few papers discussed the texture evolution in the FCC HEAs during HPT processing and its influence on the subsequent mechanical properties (Gubicza et al., 2019b; Skrotzki et al., 2020). Apart from dislocation based nano-structuring and texture evolution, the FCC HEAs can undergo FCC→HCP transformation during HPT deformation (Chandan et al., 2021a; Sathiyamoorthi et al., 2021; Skrotzki et al., 2020). Stacking fault energy (SFE) of the FCC phase influences the occurrence of various deformation characteristics including FCC→HCP transformation, that is transformation induced plasticity (TRIP), twinning induced plasticity (TWIP) and dislocation slip (Allain et al., 2004; Grässel et al., 2000; Madivala et al., 2018). A variation in the SFE-dependent deformation characteristics can greatly affect the hardness evolution in the FCC HEAs (Gubicza et al., 2019b; Skrotzki et al., 2020). Hence, it becomes vital to control the SFE of the FCC materials in order to trigger the desired deformation characteristics during HPT.

The SFE at a given temperature can be manoeuvred by modifying the composition of the alloy (Gallagher, 1970). With regards to Cantor alloy and its derivatives, numerous investigations have been carried out on the onset of different deformation characteristics under uniaxial tensile loading. Genesis of a particular deformation feature at RT was achieved by modulating the SFE of the FCC phase via compositional adjustments. Specifically, several earlier studies have shown the effect of Ni elimination from the Cantor alloy and subsequent Mn variation on the Gibbs free energy change during FCC (γ) → HCP (ε) transformation ($\Delta G^{\gamma\rightarrow\varepsilon}$) and SFE of the resultant alloy (Guo et al., 2020; Li et al., 2016b; Li and Raabe, 2017; Wei et al., 2019c). Likewise, the effect of other constituent elements such as Cr and Co has also been studied on the SFE-dependent deformation behavior (Liu et al., 2019b; Wei et al., 2019a, 2019b; Zhang et al., 2020a). Although a number of work related to compositional modifications affecting SFE/$\Delta G^{\gamma\rightarrow\varepsilon}$and the deformation mechanism during uniaxial tensile loading has been carried out (Li et al., 2016b; Nene et al., 2021; Wei et al., 2019a; Wung et al., 2018), the effect of the compositional alteration on the evolution of the plasticity mechanism during SPD such as HPT of HEAs has not been investigated till date to the best of authors' knowledge.

Accordingly, the present work investigates the microstructure and hardness evolution during HPT processing of two different Ni altered compositional subsets of Cantor alloy, (i) $Fe_{40}Mn_{40}Co_{10}Cr_{10}$ and (ii) $Fe_{35}Mn_{35}Co_{10}Cr_{10}Ni_{10}$. A detailed study has been carried out to discern the differences in the plastic deformation behavior with the different Ni contents. Further, the implication of the difference in the deformation behaviours at the different examined locations within the HPT-processed specimens are correlated with the corresponding hardness values.

2. Experimental details

Vacuum arc melting was used to produce two separate HEAs with compositions of $Fe_{40}Mn_{40}Co_{10}Cr_{10}$ and $Fe_{35}Mn_{35}Co_{10}Cr_{10}Ni_{10}$ (in atomic%), referred to as Ni0 and Ni10, respectively. Starting raw material, that is the constituent elements had a purity > 99.9%. The bulk alloys were thermomechanically processed to produce a recrystallized microstructure, and the details of the processing

procedures can be found in the supplementary material (section S1). The circular disk specimens having a diameter of 10 mm and a thickness of 0.9 mm were cut for high-pressure torsion (HPT) processing. In the present study, a quasi-constrained set-up for HPT processing was used for all samples (Zhilyaev and Langdon, 2008). Fig. 1(a) presents the schematic of HPT processing and the parameters used in the present study. In practice, a disk specimen is kept between the upper and lower anvils and a constant pressure of 6 GPa was applied to the disk. A rotation speed was kept constant at 1 rpm and a series of samples were subjected to ½, 2 and 5 complete turns. Processing was carried out at room temperature (24±1 °C). The shear strain (γ) during HPT at any locations of the disk is a function of a distance from the center of the disk (r), number of HPT rotations (n), and a thickness of the specimen (t), and it can be expressed as (Zhilyaev and Langdon, 2008):

$$\gamma = 2\pi rn/t \tag{1}$$

As per the Eq. (1), the estimated shear strains at 4 mm distance away from the disk center are deduced as 17, 87 and 251, after ½, 2 and 5 turns, respectively.

X-ray diffraction (XRD), electron backscattered diffraction (EBSD), scanning electron microscopy (SEM) and transmission electron microscopy (TEM) were employed to investigate the microstructure of the as-received and HPT-processed samples. Details of the sample preparation can be found in the supplementary material (section S2). In each processing condition, the specimens for the microstructural investigations were prepared from the central region as well as from the area at 4 mm away from the disk center (representing the periphery of the HPT-processed disk).

Fig. 1(b) shows the locations of the microstructural investigations by X-ray line profile analysis (XLPA) after HPT processing. XLPA employing convolutional multiple whole profile (CMWP) fitting was carried out on the HPT-processed samples in order to understand the evolution of the defect structures during HPT processing (Gubicza, 2014; Ribárik et al., 2004). The XRD patterns were obtained in a θ-θ geometry employing a Smartlab diffractometer (manufacturer: Rigaku, Japan) which uses a parallel beam and CuKα_1 radiation. A beam length of 2 mm was employed, where it was perpendicular to the plane of the incident and the detected scattered beams. The XRD measurements were carried out for the 2θ angle range of 35–105° with the resolution of 0.005° and at a scan speed of 0.1 °/min. A detailed description of CMWP analysis can be found in the supplementary material (section S3).

XRD investigations before HPT processing was carried out in Bruker D8 Advance diffractometer. The measurements were performed employing CuKα radiation in Bragg–Brentano geometry over the angular range of 40 to 102° using step size 0.02°and 5 s as time per step. EBSD was carried out in an FEI Nova Nano scanning electron microscope 430 operated at 20 kV. A step size of 100 nm was used for the EBSD characterization. TEM investigations were carried out using a 200 kV JEOL JEM 2200FS equipment.

Hardness measurements of the HPT-processed specimens were performed by employing a Vickers hardness tester (EMCO). A load of 500 g was applied for a dwell time of 30 s. The measurements were performed along the diameters of the HPT-processed discs at an equal interval of 1 mm. At least five indentations were performed to estimate the average hardness value at each specific distance from the disk center along five different diameters in each HPT disk.

3. Experimental results

3.1. Initial microstructure

Fig. 2 presents the initial microstructure of the Ni0 and Ni10 alloys. The indexed XRD patterns in Fig. 2(a) showed a single phase FCC structure for both alloys in the as-received condition. Fig. 2(b) and (c) present the EBSD inverse pole figure (IPF) maps of the Ni0 and Ni10 alloys, respectively. Both alloys showed polygonal FCC grains along with annealing twins. The propensity of twins was

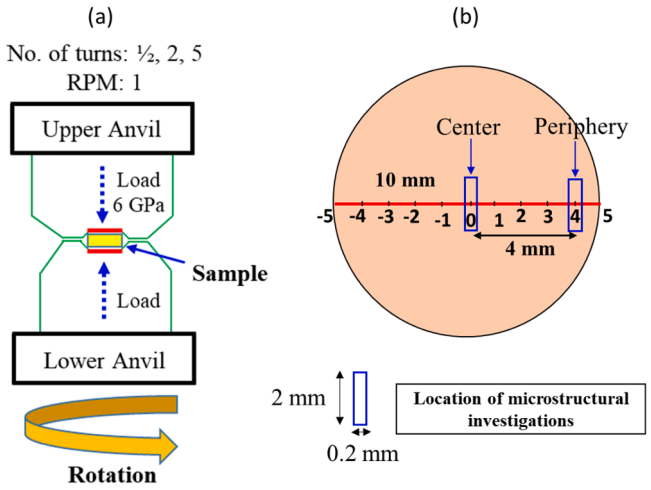

Fig. 1. (a) Schematic of HPT processing and the involved parameters; (b) the locations of the microstructural investigations after HPT processing.

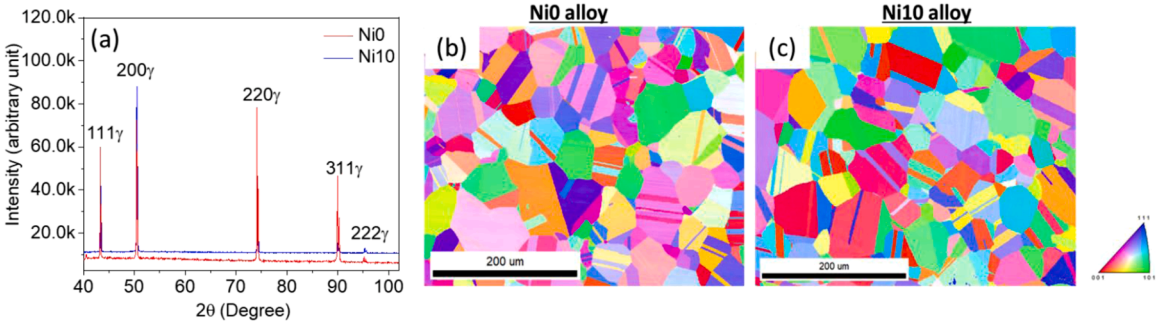

Fig. 2. (a) XRD patterns of the as-received Ni0 and Ni10 alloys. The EBSD IPF maps for the initial (b) Ni0 and (c) Ni10 alloy.

greater in the Ni0 alloy than the Ni10 alloy. The average grain sizes of the Ni0 and Ni10 alloys measured using the line intercept method (excluding the annealing twins) were 36 ± 7 μm and 48 ± 12 μm, respectively. Both alloys demonstrated similar texture as indicated by the bulk texture analysis presented in the supplementary material (section S4). Both alloys were chemically homogenous as was confirmed by SEM-energy dispersive spectroscopy (EDS) maps (shown in Figure S2 of the supplementary material).

3.2. HPT processing

3.2.1. Microstructure evolution

Fig. 3(a) and (b) present the XRD patterns of the HPT-processed Ni0 and Ni10 alloys, respectively, with increasing HPT turns. Apart from the FCC crystal structure, the HPT-processed Ni0 alloy showed additional reflections corresponding to an HCP phase, indicating the occurrence of the TRIP mechanism, that is, $\gamma \rightarrow \varepsilon$ transformation during HPT processing even after ½ turn. The newly formed HCP phase constituted the majority of the volume of the Ni0 alloy after HPT processing as was also shown in a previous study (Chandan et al., 2021a). On the other hand, the HPT-processed Ni10 alloy showed a full FCC structure except very small HCP peaks appearing after 1/2–2 HPT turns followed by a disappearance of the HCP peaks after 5 turns of HPT processing. The disappeared HCP peaks

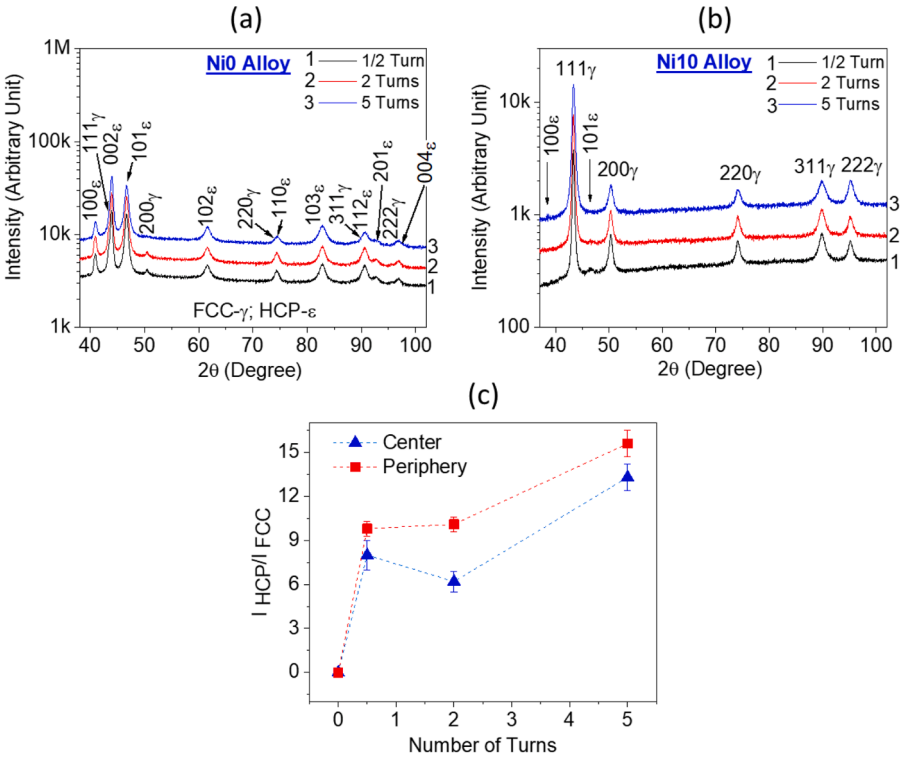

Fig. 3. XRD patterns acquired after HPT processing from the peripheries of (a) Ni0 alloy confirming the presence of the HCP phase, b) Ni10 alloy showing the FCC as the major phase with minor peaks of the HCP phase; (c) integrated intensity (I) ratio of the HCP to the FCC phase in the Ni0 alloy at the disk centers and peripheries suggesting an increasing trend of the HCP phase fraction at both locations with increasing numbers of HPT turns.

crudely ascertains that the volume fraction of the HCP phase did not increase with increasing numbers of HPT turns. The volume fraction of the HCP phase was too low to quantify in the Ni10 alloy. Fig. 3(c) shows the integrated intensity ratio of the transformed HCP phase and the original FCC phase I_{HCP}/I_{FCC} for the Ni0 alloy, where I represents the sum of the integrated intensity of all the peaks of a particular phase. I_{HCP}/I_{FCC} increased with increasing numbers of turns both at the peripheries and centers, indicating a continuous occurrence of the TRIP mechanism during HPT processing. Further, the I_{HCP}/I_{FCC} ratio was always greater at the disk peripheries than the centers, thereby signifying a greater volume fraction of the HCP phase at the periphery locations in the Ni0 alloy.

Fig. 4(a) shows a presence of deformation bands formed at the disk center after ½ turn in the Ni0 alloy. The selected area diffraction (SAD) pattern from the region shown in Fig. 4(a) was indexed with respect to the FCC and HCP phases (Fig. 4(b)), thus confirming the occurrence of $\gamma \rightarrow \varepsilon$ transformation even at the disk center after ½ turn . Fig. 4(c) presents the dark field (DF) micrograph imaged by employing the encircled diffraction spot in Fig. 4(b). Since the encircled spot corresponds to the HCP phase, only the regions transformed to the HCP phase was illuminated in the DF micrograph. Similarly, Fig. 4 (d-f) illustrate the occurrence of extensive $\gamma \rightarrow \varepsilon$ transformation in the periphery of the Ni0 alloy processed for ½ turn . The FCC and HCP phases were found to obey the following orientation relationship: $\{\bar{1}1\bar{1}\}_\gamma // \{0002_\varepsilon\}$ and $[011]_\gamma // [2\bar{1}\bar{1}0]_\varepsilon$. With increasing numbers of HPT turns, the extent of $\gamma \rightarrow \varepsilon$ transformation increased in the Ni0 alloy, as was indicated by Fig. 3(c). At the same time, grain refinement towards nano-structure was also observed in the alloy with increasing HPT turns.

At the disk center with zero theoretical shear strain in the Ni0 alloy processed for 5 turns, deformation features in the newly formed HCP phase was observed (Fig. 5(a)). The disk center did not exhibit complete nano-structuring, as is evident from the SAD pattern which showed incomplete ring formation (Fig. 5(b)). The DF micrograph in Fig. 5(c) was imaged by employing the diffraction spot '1′ in Fig. 5(b). The tendency for nano-structuring in alloy Ni0 has already been found at the periphery of the disk processed for 2 turns of HPT under similar conditions (Chandan et al., 2021a). The formation of nano-grains with a size in the order of ~100 nm was observed at the disk periphery after 5 turns of HPT processing (Fig. 5(d)). The corresponding SAD pattern showed the complete ring formation (Fig. 5(e)) and the DF micrograph in Fig. 5(f) imaged by employing the encircled diffraction spot in Fig. 5(e) demonstrates nano-grains in the Ni0 alloy. Apart from the formation of nano-structured grains, signature of dynamic recovery in the HCP phase was also observed. Fig. 5(g) shows such recovered grains having low density of dislocations, where the representative regions of the recovered grains are marked as "R" with dashed yellow boundaries. The single zone axis SAD pattern acquired over the investigated area indicates that nano-structuring has not happened in such local areas (Fig. 5(h)).

Fig. 6 presents the changes in grain size by aid of TEM DF micrographs at the disk centers and peripheries after (a)-(b) ½ turn and (c)-(d) 5 turns in the Ni0 alloy. At the center of the ½ turn specimen, the microstructure consisted of relatively coarse deformation bands with spacing varying from ~0.3 to 0.9 μm. At the periphery of the same specimen, significantly refined microstructure was observed with an average grain size of ~225 nm as shown in Fig. 6(b). With increasing numbers of HPT turns to 5, further grain refinement was observed both at the center and periphery as shown in Fig. 6(c) and (d), respectively. The average grain sizes at the

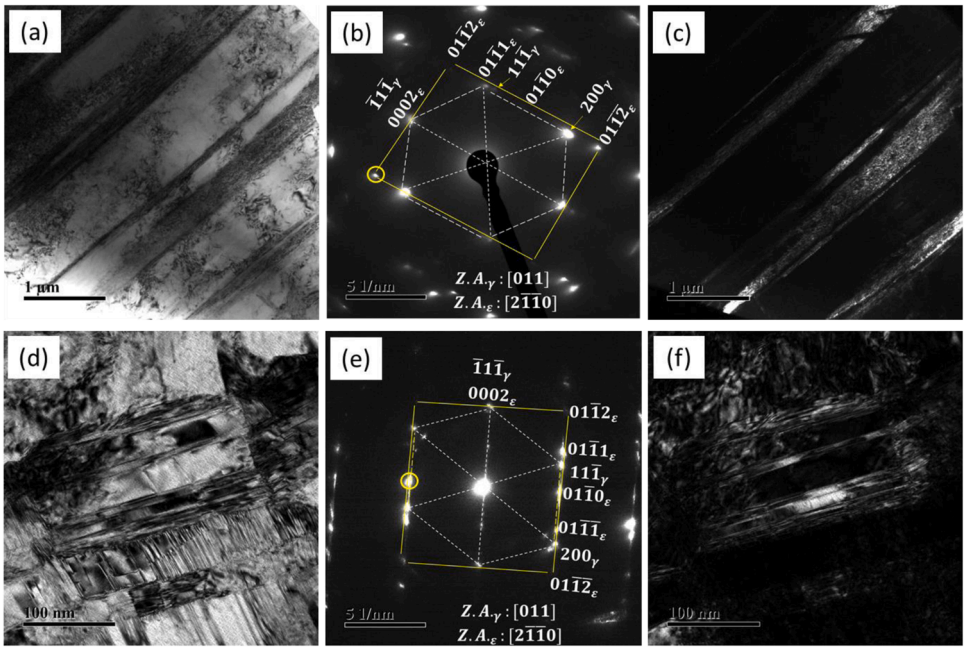

Fig. 4. Microstructure of the Ni0 alloy processed for ½ turn of HPT. (a) TEM BF micrograph at the disk center showing deformation bands; (b) corresponding SAD pattern showing the presence of both HCP and FCC phases indicating the occurrence of the TRIP effect; (c) TEM DF micrograph imaged by employing the encircled diffraction spot in figure (b); (d) TEM BF micrograph taken at the periphery indicating severe microstructural refinement compared to the center; (e) corresponding SAD pattern indexed with respect to the HCP and FCC phases; (f) TEM DF micrograph imaged by employing the encircled diffraction spot in figure (e).

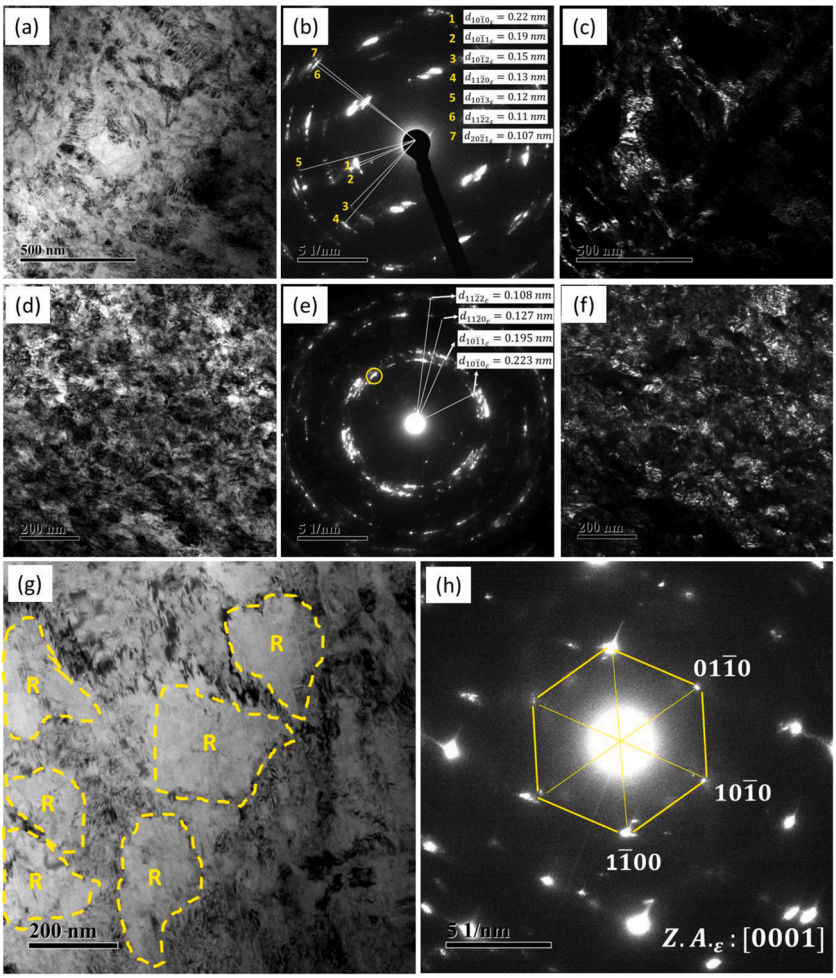

Fig. 5. Microstructure of the Ni0 alloy processed for 5 turns of HPT. (a) TEM BF micrograph at the disk center; (b) corresponding SAD pattern showing an incomplete ring formation indicating tendency towards nano-structuring; (c) TEM DF micrograph imaged by employing the diffraction spot No. 1 in figure (b); (d) TEM BF micrograph at the periphery showing extensive grain refinement; (e) corresponding SAD pattern confirming evidence of nano-structuring with the ring formation; (f) TEM DF micrograph imaged by employing the encircled diffraction spot in figure (e); (g) TEM BF micrograph at the periphery showing recovered grains; (h) corresponding SAD pattern. ('R' represents recovered regions).

center and periphery were ~170 nm and ~90 nm, respectively, for the Ni0 alloy after 5 HPT turns. The differences enable the explanation of the different appearance of an incomplete ring in the SAD pattern at the disk center but a complete SAD ring pattern at the disk peripheryas shown earlier in Fig. 5.

Fig. 7 displays the TEM micrographs of the Ni10 alloy processed for ½ turn. Fig. 7(a) presents a BF TEM micrograph from the disk center showing extensive twinning (Tw) in the FCC matrix (M). In the corresponding SAD pattern in Fig. 7(b), additional diffraction spots corresponding to twins were indexed with respect to the [011] zone axis whereas the FCC matrix was indexed with respect to the [101] zone axis. Fig. 7(c) presents the DF micrograph showing the twins which was imaged by employing the encircled diffraction spot. The TEM investigation at the periphery of the ½ turn processed specimen yielded an interesting feature of the early formation of nano-structured grains in the Ni10 alloy (Fig. 7 (d-f)). The ring in the SAD pattern acquired from the region shown in Fig. 7(d) signified the nano-grain formation (Fig. 7(e)). The DF micrograph imaged from the encircled diffraction spot further proves the formation of nano-grains (Fig. 7(f)). Additional spots corresponding to the ⟨0001⟩ reflection of the HCP phase were also present in the SAD pattern, as is indicated by the yellow arrows in Fig. 7(e).

Fig. 8(a) and (d) presents the TEM BF micrographs taken at the center and periphery, respectively, of the 5 turn processed Ni10 alloy. The SAD pattern showed a ring pattern corresponding to the multiple zone axes (Fig. 8(b)). Nano-grains in the DF micrograph are imaged by employing the marked diffraction spot (Fig. 8(c)). The extent of nano-structuring increased on traversing from the disk center to the periphery region after 5 turns of HPT processing (Fig. 8 (d-f)). Apart from nano-structuring in the FCC phase, a ring corresponding to the HCP phase was also observed in the SAD pattern (Fig. 8(e)). Such ring pattern for the HCP phase signifies the fragmentation of the earlier formed HCP phase to achieve nano-structuring which possibly contributes to hardening at the periphery of the 5 turns processed Ni10 alloy.

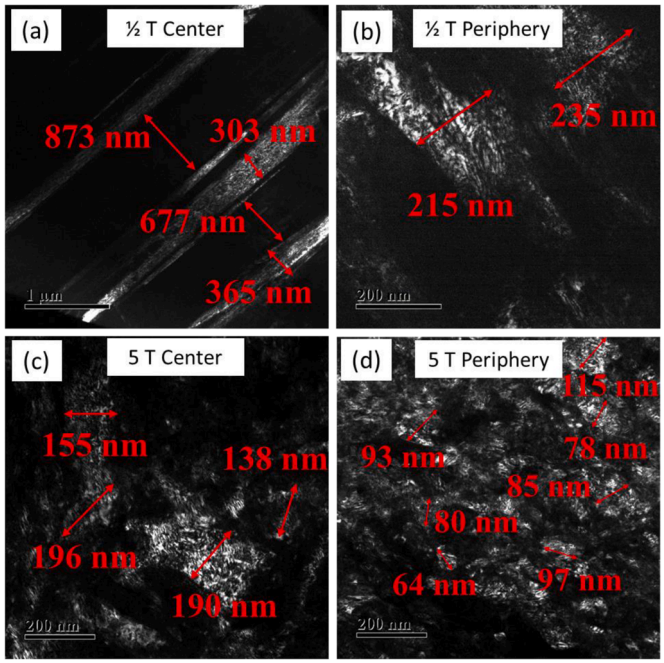

Fig. 6. DF-TEM images taken at the disk centers and peripheries of the Ni0 alloy processed for (a)-(b) ½ turn and (c)-(d) 5 HPT turns.

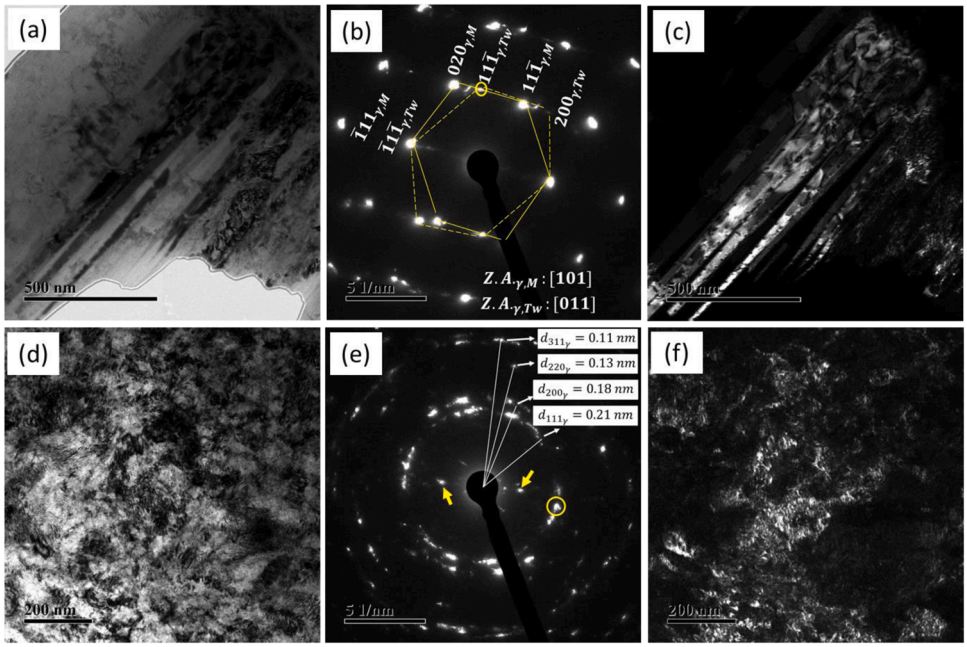

Fig. 7. Microstructure of the Ni10 alloy processed for ½ turn of HPT. (a) TEM BF micrograph taken at the disk center showing the twin formation; (b) corresponding SAD pattern; (c) TEM DF micrograph imaged by employing the encircled diffraction spot in Figure (b); (d) TEM BF micrograph taken at the periphery showing refined grains; (e) corresponding SAD pattern indicating the ring formation signifying nano-structuring; (f) TEM DF micrograph imaged by employing the encircled diffraction spot in Figure (e).

Fig. 9 presents the evolution of grain size at different investigation locations in the Ni10 alloy. Fig. 9(a) and (b) contrast the microstructures by the aid of the TEM DF micrographs between the disk center and periphery after ½ turn. The finely spaced deformation bands with ~150 nm thickness were observed at the disk center. Clearly, the deformation bands are much finer compared to the center in the Ni0 alloy after ½ turn (Fig. 6(a)). By contrast, refined grains with a grain size of 150–200 nm were observed at the periphery of the Ni10 alloy after ½ turn of HPT processing. After processing for 5 turns, grain size decreased significantly at both center and

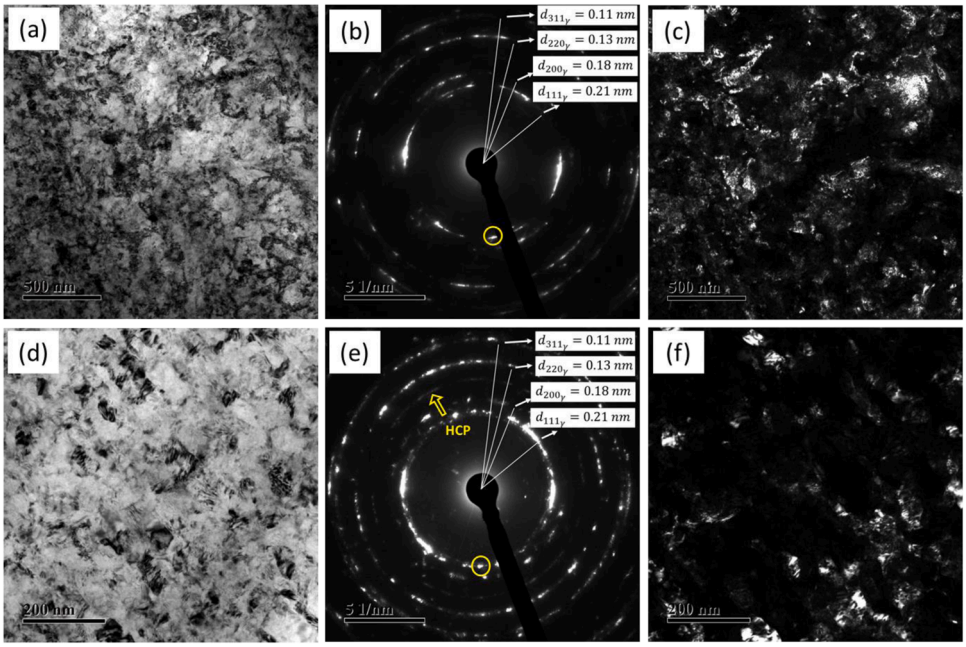

Fig. 8. Microstructure of the Ni10 alloy processed for 5 turns of HPT. (a) TEM BF micrograph taken at the disk center showing a refined microstructure; (b) corresponding SAD pattern; (c) TEM DF micrograph imaged by employing the encircled diffraction spot in the figure (b); (d) TEM BF micrograph taken at the periphery showing nano-scale grains; (e) corresponding SAD pattern indicating a ring formation from both FCC and HCP phases; (f) TEM DF micrograph imaged by employing the encircled diffraction spot in Figure (e).

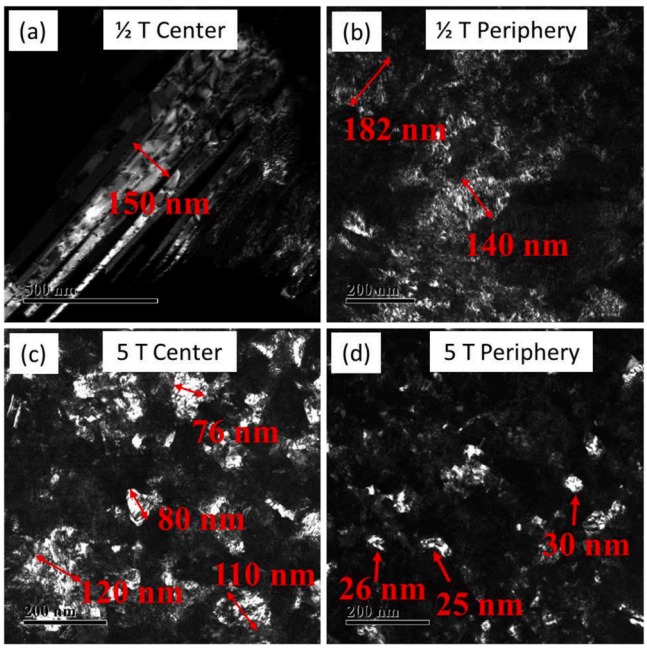

Fig. 9. TEM DF micrographs showing the evolution of grain size at the disk centers and peripheries of the Ni10 alloy with increasing numbers of HPT turns from ½ to 5.

periphery of the disk. The TEM DF micrograph in Fig. 9(c) shows that the grain size was reduced to below 100 nm at the disk center, whereas a complete nano-structuring occurred with a grain size of less than 30 nm at the periphery (see Fig. 9(d)). The results are in contrast to the Ni0 alloy, where nano-structuring in the HCP phase was not well developed and was achieved only at the peripheral region after 5 turns.

3.2.2. Microstructural characterization by XLPA

Fig. 10 shows the background subtracted and normalized (with maximum intensity) XRD peak profiles corresponding to the (102) reflection of the HCP phase taken at (a) the centers and (b) peripheries in the Ni0 alloy, and corresponding to the (200) reflection of the FCC phase at (c) the centers and (d) peripheries in the Ni10 alloy. Evidently, peak broadening in the Ni0 alloy at both centers and peripheries saturated even after ½ turn of HPT. On the other hand, the broadening of the reflection (200) peak increased monotonically at both centers and peripheries in the Ni10 alloy with increasing HPT turns. Broadening of the XRD peaks is associated with an increase in the dislocation density and/or a decrease in crystallite size. Hence, saturation in the breadth of the HCP peak suggests a saturated state of the dislocation density and/or crystallite size at both center and periphery even after ½ turn of processing in the Ni0 alloy. Saturated breadths at the center and periphery in the Ni0 alloy processed for ½ and 5 turns (shown in Fig. 11(a) and (b), respectively) indicated saturation in the dislocation density and/or crystallite size. Whereas, the saturation state could be different at the center and periphery after ½ turn in the Ni10 alloy (Fig. 11(c)) which tended towards saturation with increasing the number of turns to 5 (Fig. 11 (d)).

Williamson-Hall (WH) plots (Williamson and Hall, 1953) for both alloys presented in the supplementary material showed a non-monotonic increase in the peak broadening as a function of the magnitude of the diffraction vector for the major phases, suggesting a presence of dislocations (Figure S3 (a-b)). Quantification of the dislocation density and crystallite size at the center and periphery of both alloys was carried out by employing the CMWP fitting method. High accuracy of data fitting was obtained using CMWP which is shown in the supplementary material (Figure S3 (c-d)). Table 1 presents the evolution of the dislocation density and crystallite size during HPT for the major HCP and FCC phases in the Ni0 and Ni10 alloys, respectively. In general, both the crystallite size, $\langle x \rangle_{area}$, and dislocation density, ρ, were practically saturated at ~20 ± 5 nm and 5–7 × 10^{-15} m^{-2}, respectively, in the HCP phase at both center and peripheries in the Ni0 alloy even after the ½ turn as suggested earlier in Fig. 10(a) and (b)). Comparing these examined locations, both crystallite size and the dislocation density in the HCP phase were reasonably similar, and the tendency was also kept consistent with increasing numbers of turns of HPT turns from 1/2 to 5 in the Ni0 alloy (as was earlier indicated from Fig. 11 (a) and (b)). Regarding the FCC phase in the Ni10 alloy, crystallite size decreased without saturation through 5 turns, but the dislocation density tended to saturate after 2 turns of HPT processing. Specifically, the dislocation density of the FCC phase at the disk center was lower than at the periphery after ½ turn, but thereafter saturation in the dislocation density was noted by the similar values of ~20 × 10^{15} m^{-2} at both centers and peripheries for 2 to 5 turns. Overall, the dislocation density of the FCC phase at both centers

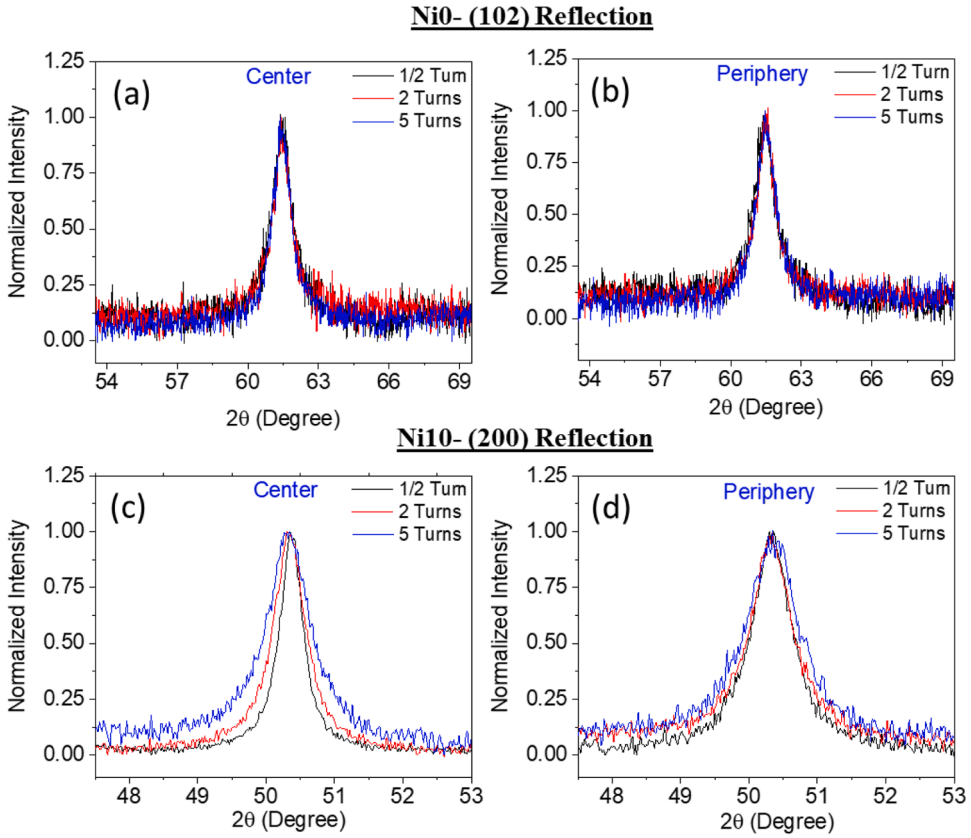

Fig. 10. Evolution of shapes of the normalized XRD peak profile with increasing numbers of HPT turns at (a) centers and (b) periphery locations corresponding to the (102) reflection of the HCP phase in the Ni0 alloy; (c) centers and (d) periphery locations corresponding to the (200) reflection of the FCC phase in the Ni10 alloy.

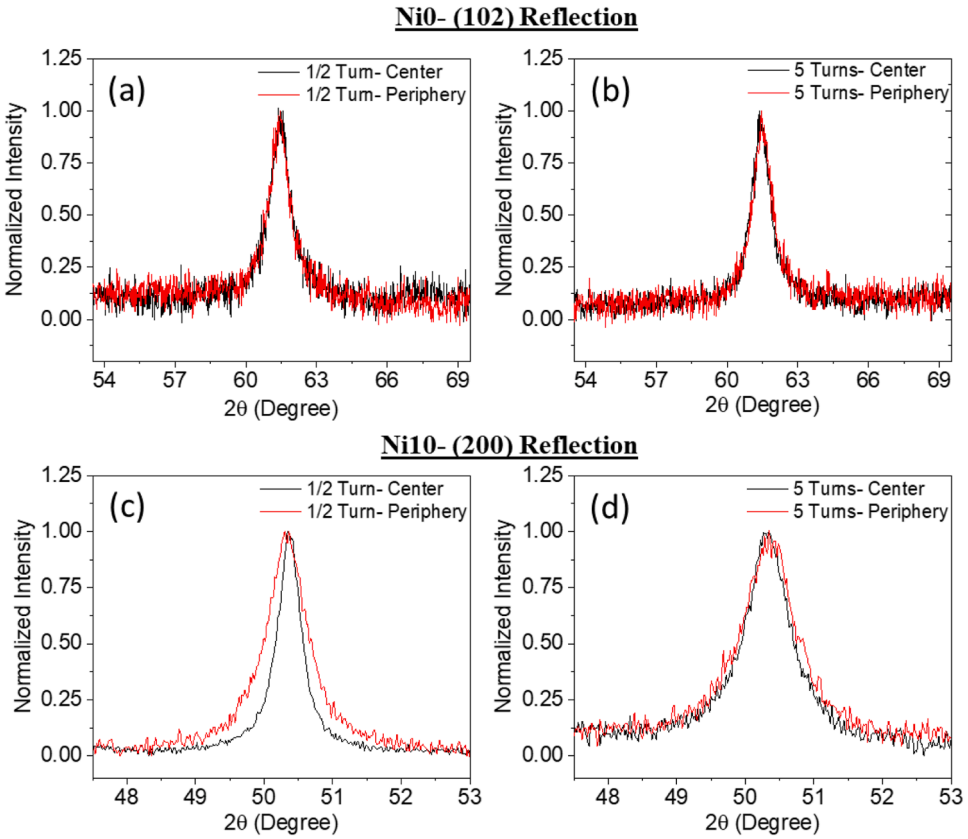

Fig. 11. Comparison of shapes of the normalized XRD peak profile at the center and periphery, corresponding to the (102) HCP reflection in the Ni0 alloy after HPT for (a) ½ turn and (b) 5 turns; corresponding to the (200) FCC reflection in the Ni10 alloy after (c) ½ turn and (d) 5 turns.

Table 1
The area-weighted mean crystallite size ($<x>_{area}$), the dislocation density (ρ) and twin fault probability (β) obtained by the CMWP fitting method for the Ni0 and Ni10 alloys.

1	Ni0 alloy		Ni10 alloy		
Samples ↓	$<x>_{area}$ [nm]	ρ [10^{15} m^{-2}]	$<x>_{area}$ [nm]	ρ [10^{15} m^{-2}]	β [%]
½ T-Center	20 ± 2	5.1 ± 0.6	49 ± 6	17.3 ± 2.0	0.6 ± 0.1
½ T-Periphery	17 ± 2	5.1 ± 0.6	34 ± 4	22.4 ± 2.5	0.5 ± 0.1
2 T-Center	17 ± 2	6.9 ± 0.8	37 ± 4	20.1 ± 2.2	0.6 ± 0.1
2 T-Periphery	16± 2	7.1 ± 0.8	30 ± 4	19.3 ± 2.1	0.6 ± 0.1
5 T-Center	22 ± 3	6.1± 0.7	27 ± 3	22.5 ± 2.4	0.8 ± 0.1
5 T-Periphery	19 =± 2	6.9 ± 0.8	24 ± 3	23.6 ± 2.5	1.0 ± 0.1

and edges in the Ni10 alloy is 3–4 times greater than that in the HCP phase in the Ni0 alloy, irrespective of the number of HPT turns. The FCC phase in the Ni10 alloy exhibited twinning which was quantified by the twin fault probability (β), where it yields the fractions of the {111} FCC planes containing twin faults. The twin fault probability remained nearly constant with the value of 0.5–0.6% up to 2 turns of HPT processing, irrespective of the locations of the investigation. Thereafter, it increased to 0.8–1% in the Ni10 alloy after HPT for 5 turns.

3.2.3. Hardness evolution

Fig. 12 presents the hardness distribution along the disk diameters of (a) the Ni0 and (b) the Ni10 alloys after HPT processing. The hardness values of the initial alloys differed only marginally: 140 (±3) Hv and 131 (±4) Hv for the Ni0 and Ni10 alloys, respectively, and these are shown by the dotted line in the plots. Both alloys demonstrated a general hardness development during HPT, where the disk centers show lower hardness which gradually increases towards the disk peripheries. Despite having similar initial hardness, the HPT-processed Ni10 alloy exhibited greater hardness at the peripheries for a given number of turns compared to the Ni0 alloy. At the disk centers after ½ turn, the hardness of the Ni10 alloy was ~19% greater than the Ni0 alloy. However, for 2 and 5 turns, the hardness at the centers was as high as ~437 Hv in the Ni0 alloy, which is in contrast to the Ni10 alloy exhibiting ~370 Hv. Hardness at the

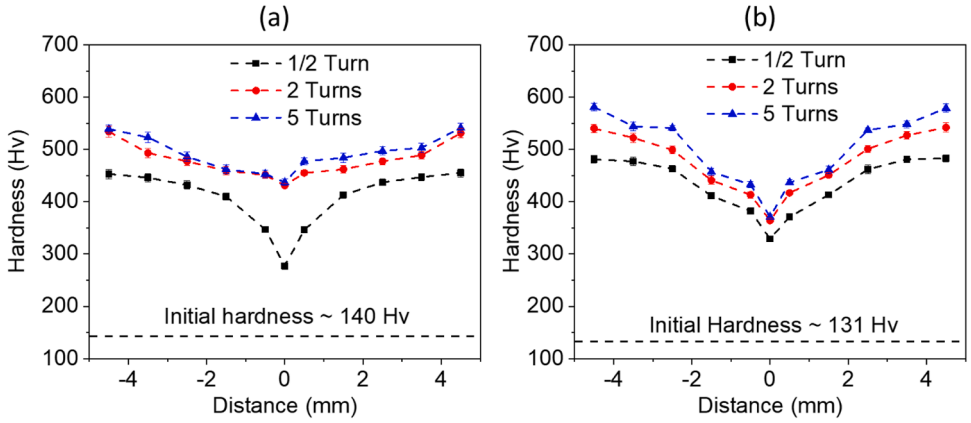

Fig. 12. Evolution of hardness along the diameters of the discs with increasing numbers of turns of HPT processing for the (a) Ni0 and (b) Ni10 alloys.

centers in the Ni10 alloy slightly increased from ~329 Hv after ½ turn to ~370 Hv after 2 turns, and it remained consistent through 5 HPT turns. This indicates there is a significant hardening behavior at the center of the Ni0 alloy when increasing HPT turns. Such hardening effect especially significant at the disk center led to attainment of near saturation in the hardness distribution along the disk diameter of the Ni0 alloy.

4. Discussion

The present work investigates the effect of Ni on the evolution of microstructure and hardness in two different variants of Cantor HEA, $Fe_{40}Mn_{40}Co_{10}Cr_{10}$ and $Fe_{35}Mn_{35}Co_{10}Cr_{10}Ni_{10}$, during HPT processing for up to 5 turns. The $Fe_{40}Mn_{40}Co_{10}Cr_{10}$ (Ni0) alloy is well-studied with respect to the plastic deformation behavior and mechanical properties (Chandan et al., 2019, 2021b, 2021a; Deng et al., 2015; He et al., 2019; Sathiyamoorthi et al., 2021; You et al., 2022). The particular alloy was developed to lower the SFE by eliminating Ni from the well-known Cantor alloy that is the equiatomic FeMnCoCrNi alloy. Lower SFE was expected to trigger mechanical twins formation in the Ni0 alloy, which was actually limited in the Cantor alloy during tensile deformation and hence was anticipated to enhance the tensile properties. However, the tensile properties of the Ni0 alloy was not improved with respect to the Cantor alloy (Chandan et al., 2019; Deng et al., 2015). This raised concern over the anticipated decrease in the SFE of the Ni0 alloy. In this context, it was recently shown that SFE of the Ni0 alloy was actually 42% higher than the Cantor alloy, which might be due to readjustments of other constituent elements after the elimination of Ni from the Cantor alloy (Chandan et al., 2021b). This raised a scientific need to understand the role of Ni on the SFE and associated deformation behavior of HEAs. Thus, a newly developed $Fe_{35}Mn_{35}Co_{10}Cr_{10}Ni_{10}$ (Ni10) alloy can foster the understanding of the role of Ni on the SFE-dependent deformation behavior of HEAs during HPT. With respect to the Ni0 alloy, the Ni10 alloy was designed such that Co and Cr content in the two alloys remain unchanged, while minor adjustments in Fe and Mn were carried out for the Ni addition. In the present study, a detailed discussion is made with respect to: (i) microstructure evolution during HPT processing and (ii) microstructure-hardness correlation after HPT processing in the two alloys.

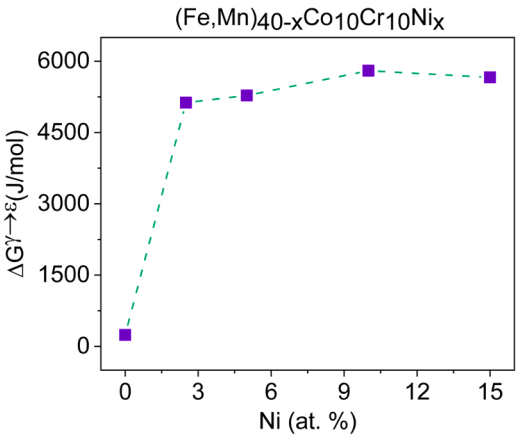

Fig. 13. Change in the Gibbs free energy for $\gamma \rightarrow \varepsilon$ transformation with the increase of the Ni content in the $(Fe,Mn)_{40\text{-}x}Co_{10}Cr_{10}Ni_x$ alloy.

4.1. Microstructure evolution during HPT processing

Significant differences in the deformation-induced microstructure were observed in the studied alloys. Specifically, the Ni0 alloy showed a significant TRIP effect, that is, FCC→HCP transformation, while the Ni10 alloy showed a limited TRIP effect during the HPT processing. The propensity of the TRIP effect increases with increasing numbers of turns for the Ni0 alloy, which contrasts with the Ni10 alloy showing a small TRIP effect only at the periphery location. To this end, in the Cantor alloy and its compositional subsets, the FCC and HCP phases are known to have comparable Gibbs free energy which leads to the negative or near zero changes in the free energy for FCC→HCP transformation ($\Delta G^{\gamma\rightarrow\varepsilon}$) (Bahramyan et al., 2020; Ma et al., 2015a; Tian et al., 2016). In such condition, the existence of both phases is equally available thermodynamically. The FCC phase being the high temperature phase is known to get retained in such HEAs in preference to the HCP phase which is considered to be the phase which only exists at lower temperatures (Ma et al., 2015b, 2015a; Zhang et al., 2014). The formation of the HCP phase is shown to be kinetically constrained and it can be formed with the aid of pressure of the order of ~14 GPa in the equiatomic Cantor alloy (Tracy et al., 2017) or at the application of severe plastic deformation such as HPT (Chandan et al., 2021a; Sathiyamoorthi et al., 2021). In the present study, $\Delta G^{\gamma\rightarrow\varepsilon}$ for the $(Fe, Mn)_{40-x}Co_{10}Cr_{10}Ni_x$ alloy was calculated by employing the TCHEA1 database in the ThermoCalc software (Andersson et al., 2002) and is presented in Fig. 13. The $\Delta G^{\gamma\rightarrow\varepsilon}$ for the Ni0 alloy (at $x = 0$) was found to be about zero. Hence, in the Ni0 alloy, the absence of HCP phase at ambient temperature, absence of transformation during tensile deformation at low stress levels, shown elsewhere (Chandan et al., 2019) and an occurrence of $\gamma \rightarrow \varepsilon$ transformation during HPT processing as shown in the present study; all these observations confirmed that a kinetic constraint existed for the HCP phase formation which actually can be overcome during HPT processing. Absence of any notable amount of HCP phase in the Ni10 alloy suggested that the applied HPT processing failed to overcome the so-called kinetic hindrance and/or the HCP phase is not thermodynamically stable in the Ni10 alloy. Fig. 13 shows that there was a prominent escalation in the $\Delta G^{\gamma\rightarrow\varepsilon}$ value in the $(Fe,Mn)_{40-x}Co_{10}Cr_{10}Ni_x$ alloy towards a more positive value with the increase in the Ni content (x). Hence, this increase in the $\Delta G^{\gamma\rightarrow\varepsilon}$ value is anticipated to prevent $\gamma \rightarrow \varepsilon$ transformation in the Ni10 alloy.

The extent of $\gamma \rightarrow \varepsilon$ transformation was different at the centers and peripheries in the Ni0 alloy. Since, $\gamma \rightarrow \varepsilon$ transformation is a strain accommodating mechanism, the transformation is expected when a load is applied and corresponding strain is produced. $\gamma \rightarrow \varepsilon$ transformation should be absent at center of the HPT disk where the shear strain is theoretically zero. However, a considerable amount of phase transformation at the disk center even after ½ turn (Fig. 3) is consistent with the significant deformation-induced microstructure evolution during HPT of many other alloys (Gubicza et al., 2019b; Heczel et al., 2017). The observed deformation-induced microstructural features at the center location in previous works is in line with the Estrin's work (Estrin et al., 2008) using the first order strain gradient plasticity model, where the model shows that a finite shear strain is accumulated even at the centers of the HPT-processed disks. Furthermore, increasing extent of the TRIP effect at the centers with an increasing numbers of turns in the present study is consistent with the model predicting ongoing accumulation of shear strain at the centers with HPT processing. The finite strain at the center can be attributed to the following reasons: (i) a compressive pressure of 6 GPa resulting in a significant strain of about 20% (Gubicza et al., 2019a)) which increases moderately with increasing numbers of turns; (ii) the XRD beam height of 2 mm averaging the information from the distance up to 1 mm on either side of the center at $r = 0$ of the disk. At the periphery of the HPT-processed disk, a higher extent of $\gamma \rightarrow \varepsilon$ transformation as seen in Fig. 3 was mainly due to a higher extent of accumulated shear strain as computed by Eq. (1).

The prevalence of TRIP effect in the Ni0 alloy during HPT is indeed expected, as in a former study a coarse-grained Ni0 alloy exhibited TRIP effect during uniaxial tensile deformation up to a strain of ~0.35, corresponding to a stress value of 500 MPa (Chandan et al., 2019). Therefore, it is expected that a much higher stress during HPT processing is enough for overcoming the critical stress required for $\gamma \rightarrow \varepsilon$ phase transformation. This critical stress is dependent on the value of $\Delta G^{\gamma\rightarrow\varepsilon}$ (He et al., 2019). Since the $\Delta G^{\gamma\rightarrow\varepsilon}$ of the Ni10 alloy is greater than that for the Ni0 alloy, the critical stress required for the $\gamma \rightarrow \varepsilon$ transformation would be higher in the Ni10 alloy, which probably was not reached during HPT processing. Therefore, the major strain accommodating mechanism in the Ni10 alloy was limited to deformation via slip and twinning. Further, a higher dislocation density in the Ni10 compared to the Ni0 alloy may be attributed to: (i) accommodation of strain by alternative deformation mechanism, viz., TRIP effect in the Ni0 alloy; (ii) prominence of the FCC phase in the Ni10 alloy having greater number of active slip system compared to the prominent HCP phase after HPT processing in Ni0 alloy, having limited number of slip system.

The magnitude of dislocation density in the Ni10 alloy was lower at the disk center than the periphery after ½ turn of HPT processing, which becomes nearly equal after processing to 2 turns and higher. The evolution of dislocation density at the center is attributed to the non-zero strain due to the reasons discussed above. On the other hand, the saturation in the dislocation density in the Ni0 alloy even after ½ turn of HPT processing can be explained by the two competing strain accommodating deformation behaviours; (i) an accommodation of strain by dislocation generation followed by slip process and (ii) a strain accommodation via $\gamma \rightarrow \varepsilon$ phase transformation. At the peripheries, the dislocation generation must be higher than the disk centers due to the greater imposed strain (including compressive and shear). However, the extent of $\gamma \rightarrow \varepsilon$ transformation is significantly higher at the peripheries than the centers, which can accommodate a substantial amount of strain (Skrotzki et al., 2020). This accommodation of strain via $\gamma \rightarrow \varepsilon$ transformation would certainly limit the generation of new dislocations at peripheries despite the larger effective strain to be accommodated. While at the center, the effective strain to be accommodated is less but at the same time the $\gamma \rightarrow \varepsilon$ transformation is also significantly lower. Further, with the increase of turns of HPT processing, again $\gamma \rightarrow \varepsilon$ transformation increases simultaneously, which again would limit the generation of new dislocations. This had rendered the dislocation density to be almost constant even with increasing the number of turns and also at the different locations. It should be noted again that due to the finite size of the XRD beam, the microstructure and phase composition obtained for the centers by XRD characterize an extended volume close to the disk center.

4.2. Microstructure-hardness correlation after HPT processing

It is evident from Fig. 12 that there is a significant variation in hardness distribution in the studied alloys after HPT. Also, the evolution in the hardness at the disk centers and peripheries is different between the two alloys. Such differences can be explained on the basis of the active deformation characteristics/strengthening mechanisms and their respective extents during HPT processing at these separate locations. Thus, discussion is confined to the centers and peripheries of the studied alloys, where Fig. 14 shows (a) the sequential variations in the deformation behavior schematically and (b) variation in hardness depending on the location (center and periphery) with increasing numbers of HPT turns. In the Ni0 alloy, the major strengthening mechanisms are: (i) second phase strengthening by the transformed HCP phase, where the HCP phase is harder and stronger than the FCC phase (Chen et al., 2020; Fang et al., 2018), (ii) Taylor hardening due to the increased dislocation density of about $5 \times 10^{15}\ m^{-2}$ (Table 1), and (iii) Hall-Petch strengthening owing to grain refinement. On the other hand, the strengthening mechanisms in the Ni10 alloy are: (i) Taylor hardening due to remarkably increased dislocation density of about $2 \times 10^{16}\ m^{-2}$ (Table 1) which is about 4 times higher than that in the Ni0 alloy, (ii) Hall-Petch strengthening, where the observed nano-scale grains are smaller in the Ni10 alloy than in the Ni0 alloy, and (iii) minor TRIP and TWIP effects.

Since the dislocation density had already saturated both at center and periphery even for ½ turn of HPT processing in the Ni0 alloy, the contribution of Taylor hardening toward the material's hardness would be similar at both locations for the alloy irrespective of the HPT turns. Herein, the lower hardness at the center compared to the periphery in the Ni0 alloy after ½ turn was mainly due to the lower fraction of the HCP phase at the central location (Fig. 14(a)) and a lower extent of grain refinement. With increasing numbers of turns from ½ to 5 in the Ni0 alloy, the difference in hardness between center and periphery is reduced from 178 to 103 Hv (Fig. 14(b)). It indicates a tendency towards microstructural homogeneity, while it is not yet achieved completely in the present processing condition. The lack of homogeneity in hardness even after 5 turns processing is due to the higher extent of the TRIP effect coupled with higher extent of grain refinement at the periphery compared to the center. Additionally, the decreased difference in hardness between center and periphery for 5 turn processed Ni0 alloy compared to ½ turn may also be attributed to the co-occurrence of dynamic recovery at the periphery for 5 turns (Fig. 14(a)), which would have offset the hardening contributions from HCP phase and nano-structuring.

In the Ni10 alloy after ½ turn, the contribution from the Taylor hardening towards the hardness improvement would have slightly increased at the periphery compared to the center, owing to the corresponding marginal increase in the dislocation density (Table 1).

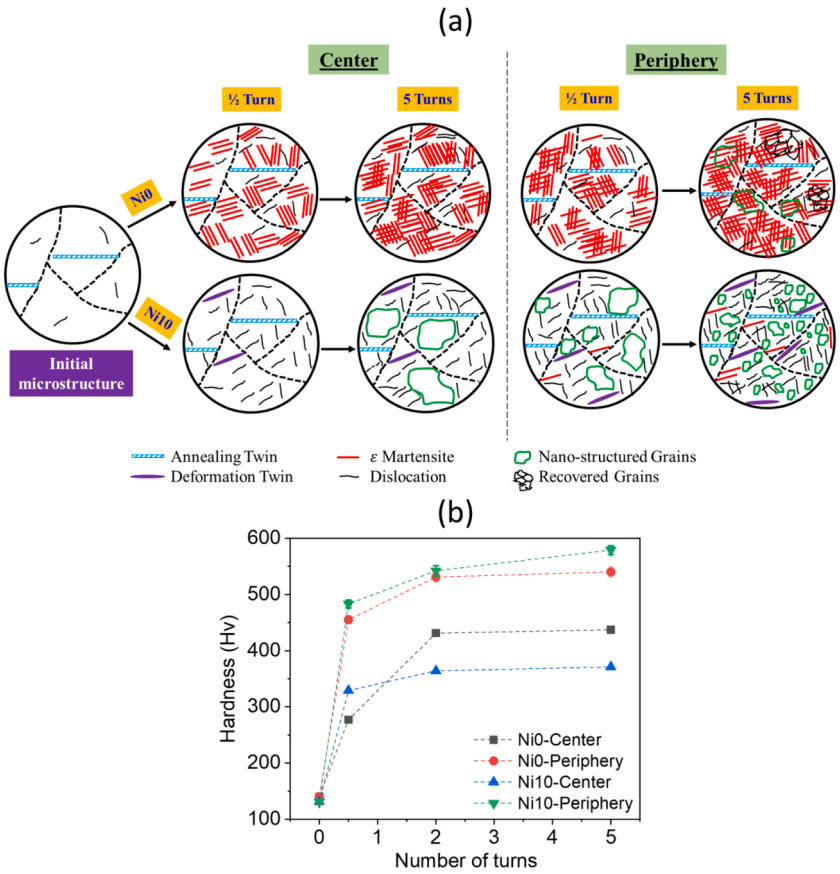

Fig. 14. (a) Schematic of the evolution of various microstructural features; (b) hardness evolution at the centers and peripheries with increasing numbers of HPT turns for the Ni0 and Ni10 alloys.

The occurrence of twinning remained similar at the centers and peripheries (Table 1). Further, an additional TRIP mechanism was active at the periphery of the ½ turn processed specimen but this effect was marginal. A substantial grain refinement (Hall-Petch strengthening) at the periphery was also observed in comparison to the central location. Hence, an increased Taylor hardening, greater Hall-Petch strengthening and a slight TRIP effect (Fig. 14(a)) resulted in the greater hardness at the periphery as compared to the center after ½ turn (Fig. 14(b)). On increasing numbers of turns to 5 in the Ni10 alloy, a considerable increase in hardness was observed at the periphery, whereas only a marginal increase was noted at the center (Fig. 14(b)). The increase in the mean hardness from 483 to 579 Hv at the periphery is attributed to the increased accumulation of strain resulting in a significant nano-structuring along with the considerable TWIP effect (Fig. 14(a)). In contrast, a slight increment in hardness at the center from 329 to 371 Hv (Fig. 14(b)) with increasing numbers of turns to 5 was mainly due to the refinement of microstructure and twinning (Fig. 14(a)).

From the viewpoint of plasticity mechanism-based alloy design of HEAs, the present study suggests that addition of Ni to the $Fe_{40}Mn_{40}Co_{10}Cr_{10}$ alloy can substantially alter the primary deformation mechanism from TRIP to dislocation mediated slip and twinning. Such an alteration in deformation mechanism is a direct consequence of shifting of $\Delta G^{\gamma\rightarrow\varepsilon}$ towards more positive value with Ni addition that is likely to prevent the TRIP effect. Further, it is important to note that the presence of a large fraction of the hard HCP phase originating from the TRIP effect does not ensures greater strengthening, instead the other competing hardening contributions such as a formation of high dislocation density and grain refinement leading to nano-structuring have major roles to play. The addition of Ni has in fact promoted a greater extent of nano-structuring in the $Fe_{35}Mn_{35}Co_{10}Cr_{10}Ni_{10}$ alloy, and thus the present results are promising to contribute to the future HEAs' compositional and microstructural designing.

Conclusions

The present work investigates the effect of Ni on the evolution of microstructure and hardness in two variants of Cantor HEA, $Fe_{40}Mn_{40}Co_{10}Cr_{10}$ (Ni0 alloy) and $Fe_{35}Mn_{35}Co_{10}Cr_{10}Ni_{10}$ (Ni10 alloy), during HPT processing for up to 5 turns under 6 GPa. Followings are the major findings in the present work:

1. Despite same crystal structure (FCC) in the initial condition irrespective of the Ni content, a prominent difference in the plasticity mechanism during HPT processing was observed in the studied alloys. The Ni0 alloy underwent an extensive TRIP effect during HPT processing rendering the transformed HCP phase as the major phase in the HPT-processed state. By contrast, the TRIP effect was limited in the Ni10 alloy. The limited TRIP effect in the Ni10 alloy is due to the increased $\Delta G^{\gamma\rightarrow\varepsilon}$ towards more positive value.
2. The major strengthening mechanisms in the Ni0 alloy were the TRIP effect, Taylor hardening in the HCP phase and grain refinement. By contrast, the Ni10 alloy displayed strengthening due to Taylor hardening, extensive nano-structuring, twinning and limited TRIP effects.
3. Despite the major differences in the deformation mechanisms for the studied alloys, a saturation in dislocation density was noted at a relatively early stage of HPT deformation (½ turn for the Ni0 alloy and 2 turns for the Ni10 alloy). In general, for any given location and processing condition, the dislocation density in the FCC phase of the Ni10 alloy ($2 \times 10^{16}\ m^{-2}$) was 4 times greater than for the HCP phase in the Ni0 alloy ($5 \times 10^{15}\ m^{-2}$).
4. Both alloys showed prominent grain refinement owing to large strain associated with HPT processing. But, the extent of grain refinement and nano-structuring was greater in the Ni10 alloy compared to the Ni0 alloy. The lesser extent of grain refinement in Ni0 alloy is due to the alternative strain accommodation by the TRIP effect.
5. Hardness at the peripheries for any given turn of HPT processing was always greater for the Ni10 alloy as compared to the Ni0 alloy due to prominence of nano-structuring and a possible contribution from the very high dislocation density.

Data availability statement

The original data for any purpose cannot be shared at the moment as these also forms part of an ongoing study.

CRediT authorship contribution statement

Avanish Kumar Chandan: Conceptualization, Data curation, Formal analysis, Investigation, Writing – original draft, Visualization, Funding acquisition, Writing – review & editing. **Kaushal Kishore:** Conceptualization, Data curation, Formal analysis, Investigation, Writing – original draft, Visualization, Funding acquisition, Writing – review & editing. **Pham Tran Hung:** Data curation, Investigation. **Mainak Ghosh:** Investigation, Writing – review & editing. **Sandip Ghosh Chowdhury:** Formal analysis, Investigation, Writing – review & editing. **Megumi Kawasaki:** Formal analysis, Investigation, Writing – original draft, Writing – review & editing. **Jenő Gubicza:** Conceptualization, Supervision, Writing – original draft, Writing – review & editing.

Declaration of Competing Interest

The authors declare that they have no known competing financial interests or personal relationships that could have appeared to influence the work reported in this paper.

Acknowledgment

The necessary funds and equipment support for carrying out the present work was provided by CSIR-National Metallurgical Laboratory, India, under the *i*-PSG initiative; Project number: OLP 0346. A part of this work was carried out under the National Science Foundation of the United States under Grant No. DMR-1810343.

Supplementary materials

Supplementary material associated with this article can be found, in the online version, at doi:10.1016/j.ijplas.2021.103193.

References

Allain, S., Chateau, J.P., Bouaziz, O., Migot, S., Guelton, N., 2004. Correlations between the calculated stacking fault energy and the plasticity mechanisms in Fe-Mn-C alloys. Mater. Sci. Eng. A 387–389, 158–162. https://doi.org/10.1016/j.msea.2004.01.059.

Andersson, J.-O., Helander, T., Hoglund, L., Pingfang, S., Sundman, B., 2002. THERMO-CALC & DICTRA, computational tools for materials science. Calphad 26, 273–312. https://doi.org/10.1016/S0364-5916(02)00037-8.

Asghari-rad, P., Sathiyamoorthi, P., Bae, J.W., Moon, J., Park, J.M., Zargaran, A., Kim, H.S., 2019. Effect of grain size on the tensile behavior of V10Cr15Mn5Fe 35Co10Ni25 high entropy alloy. Mater. Sci. Eng. A 744, 610–617. https://doi.org/10.1016/j.msea.2018.12.077.

Bahramyan, M., Mousavian, R.T., Brabazon, D., 2020. Study of the plastic deformation mechanism of TRIP – TWIP high entropy alloys at the atomic level. Int. J. Plast. 127, 102649 https://doi.org/10.1016/j.ijplas.2019.102649.

Cantor, B., Chang, I.T.H., Knight, P., Vincent, A.J.B., 2004. Microstructural development in equiatomic multicomponent alloys. Mater. Sci. Eng. A 375–377, 213–218. https://doi.org/10.1016/j.msea.2003.10.257.

Chandan, A.K., Hung, P.T., Kishore, K., Kawasaki, M., Chakraborty, J., Gubicza, J., 2021a. On prominent TRIP effect and non-basal slip in a TWIP high entropy alloy during high-pressure torsion processing. Mater. Charact. 178, 111284 https://doi.org/10.1016/j.matchar.2021.111284.

Chandan, A.K., Tripathy, S., Ghosh, M., Chowdhury, S.G., 2019. Evolution of Substructure of a non-equiatomic FeMnCrCo high entropy alloy deformed at ambient temperature. Metall. Mater. Trans. A 50, 5079–5090. https://doi.org/10.1007/s11661-019-05438-z.

Chandan, A.K., Tripathy, S., Sen, B., Ghosh, M., Chowdhury, S.G., 2021b. Temperature dependent deformation behavior and stacking fault energy of Fe40Mn40Co10Cr10 alloy. Scr. Mater. 199, 113891 https://doi.org/10.1016/j.scriptamat.2021.113891.

Chen, S., Oh, H.S., Gludovatz, B., Kim, S.J., Park, E.S., Zhang, Z., Ritchie, R.O., Yu, Q., 2020. Real-time observations of TRIP-induced ultrahigh strain hardening in a dual-phase CrMnFeCoNi high-entropy alloy. Nat. Commun. 11, 826. https://doi.org/10.1038/s41467-020-14641-1.

Deng, Y., Tasan, C.C., Pradeep, K.G., Springer, H., Kostka, A., Raabe, D., 2015. Design of a twinning-induced plasticity high entropy alloy. Acta Mater. 94, 124–133. https://doi.org/10.1016/j.actamat.2015.04.014.

Ding, Z.Y., He, Q.F., Wang, Q., Yang, Y., 2018. Superb strength and high plasticity in laves phase rich eutectic medium-entropy-alloy nanocomposites. Int. J. Plast. 106, 57–72. https://doi.org/10.1016/j.ijplas.2018.03.001.

Estrin, Y., Molotnikov, A., Davies, C.H.J., Lapovok, R., 2008. Strain gradient plasticity modelling of high-pressure torsion. J. Mech. Phys. Solids 56, 1186–1202. https://doi.org/10.1016/j.jmps.2007.10.004.

Fang, Q., Chen, Y., Li, J., Jiang, C., Liu, B., Liu, Y., Liaw, P.K., 2018. Probing the phase transformation and dislocation evolution in dual-phase high-entropy alloys. Int. J. Plast. https://doi.org/10.1016/j.ijplas.2018.10.014.

Gallagher, P.C.J., 1970. The influence of alloying, temperature, and related effects on the stacking fault energy. Metall. Trans. 1, 2429–2461. https://doi.org/10.1007/BF03038370.

Gludovatz, B., Hohenwarter, A., Catoor, D., Chang, E.H., George, E.P., Ritchie, R.O., 2014. A fracture-resistant high-entropy alloy for cryogenic applications. Science 345, 1153–1158. https://doi.org/10.1126/science.1254581.

Gludovatz, B., Hohenwarter, A., Thurston, K.V.S., Bei, H., Wu, Z., George, E.P., Ritchie, R.O., 2016. Exceptional damage-tolerance of a medium- entropy alloy CrCoNi at cryogenic temperatures. Nat. Commun. 7, 10602. https://doi.org/10.1038/ncomms10602.

Grässel, O., Krüger, L., Frommeyer, G., Meyer, L.W., 2000. High strength Fe-Mn-(Al, Si) TRIP/TWIP steels development - properties - application. Int. J. Plast. 16, 1391–1409. https://doi.org/10.1016/S0749-6419(00)00015-2.

Gubicza, J., 2014. X-Ray Line Profile Analysis in Materials Science, 1st ed. IGI Global.

Gubicza, J., Heczel, A., Kawasaki, M., Han, J., Zhao, Y., Xue, Y., Huang, S., Labar, J.L., 2019a. Evolution of microstructure and hardness in Hf25Nb25Ti25Zr25 high-entropy alloy during high-pressure torsion. J. Alloys Compd. 788, 318–328. https://doi.org/10.1016/j.jallcom.2019.02.220.

Gubicza, J., Tran, P., Kawasaki, M., Han, J., Zhao, Y., Xue, Y., Labar, J.L., 2019b. Influence of severe plastic deformation on the microstructure and hardness of a CoCrFeNi high-entropy alloy : a comparison with CoCrFeNiMn. Mater. Charact. 154, 304–314. https://doi.org/10.1016/j.matchar.2019.06.015.

Guo, W., Su, J., Lu, W., Liebscher, C.H., Kirchlechner, C., Ikeda, Y., Körmann, F., Liu, X., Xue, Y., Dehm, G., 2020. Dislocation-induced breakthrough of strength and ductility trade-off in a non-equiatomic high-entropy alloy. Acta Mater. 185, 45–54. https://doi.org/10.1016/j.actamat.2019.11.055.

He, Z.F., Jia, N., Ma, D., Yan, H.L., Li, Z.M., Raabe, D., 2019. A Joint contribution of transformation and twinning to the high strength- ductility combination of a FeMnCoCr high entropy alloy at cryogenic temperatures. Mater. Sci. Eng. A 759, 437–447. https://doi.org/10.1016/j.msea.2019.05.057.

Heczel, A., Kawasaki, M., Labar, J.L., Jang, J., Langdon, T.G., Gubicza, J., 2017. Defect structure and hardness in nanocrystalline CoCrFeMnNi High- entropy alloy processed by high-pressure torsion. J. Alloys Compd. 711, 143–154. https://doi.org/10.1016/j.jallcom.2017.03.352.

Li, J., Chen, H., Fang, Q., Jiang, C., Liu, Y., Liaw, K., 2020. Unraveling the dislocation – precipitate interactions in high-entropy alloys. Int. J. Plast. 133, 102819 https://doi.org/10.1016/j.ijplas.2020.102819.

Li, J., Jia, W., Wang, J., Kou, H., Zhang, D., Beaugnon, E., 2016a. Enhanced mechanical properties of a CoCrFeNi high entropy alloy by supercooling method. Mater. Des. 95, 183–187. https://doi.org/10.1016/j.matdes.2016.01.112.

Li, Z., Pradeep, K.G., Deng, Y., Raabe, D., Tasan, C.C., 2016b. Metastable high-entropy dual-phase alloys overcome the strength-ductility trade-off. Nature 534, 227–230. https://doi.org/10.1038/nature17981.

Li, Z., Raabe, D., 2017. Strong and Ductile Non-equiatomic High-Entropy Alloys : design, Processing, Microstructure, and Mechanical Properties. JOM 69, 2099–2106. https://doi.org/10.1007/s11837-017-2540-2.

Liu, K., Nene, S.S., Frank, M., Sinha, S., Mishra, R.S., 2019a. Extremely high fatigue resistance in an ultrafine grained high entropy alloy. Appl. Mater. Today 15, 525–530. https://doi.org/10.1016/j.apmt.2019.04.001.

Liu, S.F., Wu, Y., Wang, H.T., Lin, W.T., Shang, Y.Y., Liu, J.B., An, K., Liu, X.J., Wang, H., Lu, Z.P., 2019b. Transformation-reinforced high-entropy alloys with superior mechanical properties via tailoring stacking fault energy. J. Alloys Compd. 792, 444–455. https://doi.org/10.1016/j.jallcom.2019.04.035.

Ma, D., Grabowski, B., Körmann, F., Neugebauer, J., Raabe, D., 2015a. Ab initio thermodynamics of the CoCrFeMnNi high entropy alloy : importance of entropy contributions beyond the configurational one. Acta Mater. 100, 90–97. https://doi.org/10.1016/j.actamat.2015.08.050.

Ma, D., Yao, M., Pradeep, K.G., Tasan, C.C., Springer, H., Raabe, D., 2015b. Phase stability of non-equiatomic CoCrFeMnNi high entropy alloys. Acta Mater. 98, 288–296. https://doi.org/10.1016/j.actamat.2015.07.030.

Madivala, M., Schwedt, A., Wong, S.L., Roters, F., Prahl, U., Bleck, W., 2018. Temperature dependent strain hardening and fracture behavior of TWIP steel. Int. J. Plast. 104, 80–103. https://doi.org/10.1016/j.ijplas.2018.02.001.
Miao, J., Slone, C.E., Smith, T.M., Niu, C., Bei, H., Ghazisaeidi, M., Pharr, G.M., Mills, M.J., 2017. The evolution of the deformation substructure in a Ni-Co-Cr equiatomic solid solution alloy. Acta Mater. 132, 35–48. https://doi.org/10.1016/j.actamat.2017.04.033.
Ming, K., Bi, X., Wang, J., 2019. Strength and ductility of CrFeCoNiMo alloy with hierarchical microstructures. Int. J. Plast. 255–268. https://doi.org/10.1016/j.ijplas.2018.10.005.
Ming, K., Bi, X., Wang, J., 2018. Realizing strength-ductility combination of coarse-grained Al0.2Co1.5CrFeNi1.5Ti0.3 alloy via nano-sized, coherent precipitates. Int. J. Plast. 100, 177–191. https://doi.org/10.1016/j.ijplas.2017.10.005.
Miracle, D.B., Senkov, O.N., 2017. A critical review of high entropy alloys and related concepts. Acta Mater. 122, 448–511. https://doi.org/10.1016/j.actamat.2015.06.025.
Nene, S.S., Agrawal, P., Frank, M., Watts, A., Shukla, S., Morphew, C., Chesetti, A., Park, J.S., Mishra, R.S., 2021. Transformative high entropy alloy conquers the strength-ductility paradigm by massive interface strengthening. Scr. Mater. 203, 114070 https://doi.org/10.1016/j.scriptamat.2021.114070.
Nene, S.S., Frank, M., Liu, K., Sinha, S., Mishra, R.S., Mcwilliams, B.A., Cho, K.C., 2019. Corrosion-resistant high entropy alloy with high strength and ductility. Scr. Mater. 166, 168–172. https://doi.org/10.1016/j.scriptamat.2019.03.028.
Nene, S.S., Liu, K., Sinha, S., Frank, M., Williams, S., Mishra, R.S., 2020. Superplasticity in fine grained dual phase high entropy alloy. Materialia 9, 100521. https://doi.org/10.1016/j.mtla.2019.100521.
Nene, S.S., Sinha, S., Frank, M., Liu, K., Mishra, R.S., Mcwilliams, B.A., Cho, K.C., 2018. Unexpected strength – ductility response in an annealed, metastable, high-entropy alloy. Appl. Mater. Today 13, 198–206. https://doi.org/10.1016/j.apmt.2018.09.002.
Nguyen, N.T., Asghari-rad, P., Sathiyamoorthi, P., Zargaran, A., Lee, C.S., Kim, H.S., 2020. Ultrahigh high-strain-rate superplasticity in a nanostructured high-entropy alloy. Nat. Commun. 11, 2736. https://doi.org/10.1038/s41467-020-16601-1.
Praveen, S., Wung, J., Asghari-rad, P., Park, J.M., Seop, H., 2018b. Ultra-high tensile strength nanocrystalline CoCrNi equi-atomic medium entropy alloy processed by high-pressure torsion. Mater. Sci. Eng. A 735, 394–397. https://doi.org/10.1016/j.msea.2018.08.079.
Reddy, S.R., Bapari, S., Bhattacharjee, P.P., Chokshi, A.H., 2017. Superplastic-like flow in a fine-grained equiatomic CoCrFeMnNi high-entropy alloy. Mater. Res. Lett. ISSN 5, 408–414. https://doi.org/10.1080/21663831.2017.1305460.
Ribárik, G., Gubicza, J., Ungár, T., 2004. Correlation between strength and microstructure of ball-milled Al-Mg alloys determined by X-ray diffraction. Mater. Sci. Eng. A 387–389, 343–347. https://doi.org/10.1016/j.msea.2004.01.089.
Sathiyamoorthi, P., Asghari-rad, P., Karthik, G.M., Alireza, Z., Kim, H.S., 2021. Unusual strain-induced martensite and absence of conventional grain refinement in twinning induced plasticity high-entropy alloy processed by high-pressure torsion. Mater. Sci. Eng. A 803, 140570. https://doi.org/10.1016/j.msea.2020.140570.
Schneider, M., George, E.P., Manescau, T.J., Záležák, T., Hunfeld, J., Dlouhý, A., Eggeler, G., Laplanche, G., 2020. Analysis of strengthening due to grain boundaries and annealing twin boundaries in the CrCoNi medium-entropy alloy. Int. J. Plast. 124, 155–169. https://doi.org/10.1016/j.ijplas.2019.08.009.
Schuh, B., Mendez-martin, F., Völker, B., George, E.P., Clemens, H., Pippan, R., Hohenwarter, A., 2015. Mechanical properties, microstructure and thermal stability of a nanocrystalline CoCrFeMnNi high-entropy alloy after severe plastic deformation. Acta Mater. 96, 258–268. https://doi.org/10.1016/j.actamat.2015.06.025.
Shahmir, H., Mousavi, T., He, J., Lu, Z., Kawasaki, M., Langdon, T.G., 2017. Microstructure and properties of a CoCrFeNiMn high-entropy alloy processed by equal-channel angular pressing. Mater. Sci. Eng. A 705, 411–419. https://doi.org/10.1016/j.msea.2017.08.083.
Sinha, S., Nene, S.S., Frank, M., Liu, K., Agrawal, P., Mishra, R.S., 2019. On the evolving nature of c/a ratio in a hexagonal close-packed epsilon martensite phase in transformative high entropy alloys. Sci. Rep. 9, 13185. https://doi.org/10.1038/s41598-019-49904-5.
Skrotzki, W., Pukenas, A., Odor, E., Joni, B., Ungar, T., Völker, B., Hohenwarter, A., Pippan, R., George, E.P., 2020. Microstructure, texture, and strength development during high-pressure torsion of CrMnFeCoNi high-entropy alloy. Crystals 10, 336. https://doi.org/10.3390/cryst10040336.
Srivastan, T.S., Gupta, M., 2020. High entropy alloys: innovations, advances, and applications. In: Bansal, G.K., Chandan, A.K., Mandal, G.K., Srivastava, V.C. (Eds.), High Entropy Alloys: An Overview on Current Developments. CRC Press, Boca Raton. https://doi.org/10.1201/9780367374426-1.
Thapliyal, S., Nene, S.S., Agrawal, P., Wang, T., Morphew, C., Mishra, R.S., Mcwilliams, B.A., Cho, K.C., 2020. Damage-tolerant, corrosion-resistant high entropy alloy with high strength and ductility by laser powder bed fusion additive manufacturing. Addit. Manuf. 36, 101455 https://doi.org/10.1016/j.addma.2020.101455.
Tian, F., Károly, L., Shen, J., Vitos, L., 2016. Calculating elastic constants in high-entropy alloys using the coherent potential approximation : current issues and errors. Comput. Mater. Sci. 111, 350–358. https://doi.org/10.1016/j.commatsci.2015.09.058.
Tong, Y., Chen, D., Han, B., Wang, J., Feng, R., Yang, T., Zhao, C., Zhao, Y.L., Guo, W., Shimizu, Y., Liu, C.T., Liaw, P.K., Inoue, K., Nagai, Y., Hu, A., Kai, J.J., 2019. Outstanding tensile properties of a precipitation-strengthened FeCoNiCrTi 0.2 high-entropy alloy at room and cryogenic temperatures. Acta Mater. 165, 228–240. https://doi.org/10.1016/j.actamat.2018.11.049.
Tracy, C.L., Park, S., Rittman, D.R., Zinkle, S.J., Bei, H., Lang, M., Ewing, R.C., Mao, W.L., 2017. High pressure synthesis of a hexagonal close-packed phase of the high-entropy alloy CrMnFeCoNi. Nat. Commun. 8, 1–6. https://doi.org/10.1038/ncomms15634.
Valiev, R.Z., Islamgaliev, R.K., Alexandrov, I.V., 2000. Bulk nanostructured materials from severe plastic deformation. Prog. Mater. Sci. 45, 103–189. https://doi.org/10.1016/S0079-6425(99)00007-9.
Wang, T., Shukla, S., Gwalani, B., Sinha, S., Thapliyal, S., Frank, M., Mishra, R.S., 2021. Co - introduction of precipitate hardening and TRIP in a TWIP high - entropy alloy using friction stir alloying. Sci. Rep. 11, 1579. https://doi.org/10.1038/s41598-021-81350-0.
Wei, S., Kim, J., Tasan, C.C., 2019c. Boundary micro-cracking in metastable Fe45Mn35Co10Cr10 high-entropy alloys. Acta Mater. 168, 76–86. https://doi.org/10.1016/j.actamat.2019.01.036.
Wei, D., Li, X., Heng, W., Koizumi, Y., He, F., Choi, W.-.M., Lee, B., Kim, H.S., Kato, H., Chiba, A., 2019a. Novel Co-rich high entropy alloys with superior tensile properties. Mater. Res. Lett. 7, 82–88. https://doi.org/10.1080/21663831.2018.1553803.
Wei, D., Li, X., Jiang, J., Heng, W., Koizumi, Y., Choi, W., Lee, B., Seop, H., Kato, H., Chiba, A., 2019b. Novel Co-rich high performance twinning-induced plasticity (TWIP) and transformation-induced plasticity (TRIP) high-entropy alloys. Scr. Mater. 165, 39–43. https://doi.org/10.1016/j.scriptamat.2019.02.018.
Williamson, G., Hall, W., 1953. X-ray line broadening from filed aluminium and Wolfram. Acta Metall. 1, 22–31. https://doi.org/10.1016/0001-6160(53)90006-6.
Wung, J., Bok, J., Moon, J., Su, S., Ji, M., Yong, H., Lee, B., Seop, H., 2018. Exceptional phase-transformation strengthening of ferrous medium- entropy alloys at cryogenic temperatures. Acta Mater. 161, 388–399. https://doi.org/10.1016/j.actamat.2018.09.057.
Yeh, J., Chen, S., Lin, S., Gan, J., Chin, T., Shun, T., Tsau, C., 2004. Nanostructured high-entropy alloys with multiple principal elements : novel alloy design concepts and outcomes. Adv. Eng. Mater. 6, 299–303. https://doi.org/10.1002/adem.200300567.
You, D., Yang, G., Choa, Y., Kim, J., 2022. A Crack-resistant σ /FCC interfaces in the Fe40Mn40Co10Cr10 high entropy alloy with the dispersed σ -phase. Mater. Sci. Eng. A 831, 142039. https://doi.org/10.1016/j.msea.2021.142039.
Zhang, F., Zhang, C., Chen, S.L., Zhu, J., Cao, W.S., Kattner, U.R., 2014. CALPHAD : computer coupling of phase diagrams and thermochemistry an understanding of high entropy alloys from phase diagram calculations. Calphad 45, 1–10. https://doi.org/10.1016/j.calphad.2013.10.006.
Zhang, H.F., Yan, H.L., Yu, H., Ji, Z.W., Hu, Q.M., Jia, N., 2020a. The effect of Co and Cr substitutions for Ni on mechanical properties and plastic deformation mechanism of FeMnCoCrNi high entropy alloys. J. Mater. Sci. Technol. 48, 146–155. https://doi.org/10.1016/j.jmst.2020.03.010.
Zhang, T.W., Ma, S.G., Zhao, D., Wu, Y.C., Zhang, Y., Wang, Z.H., Qiao, J.W., 2020b. Simultaneous enhancement of strength and ductility in a NiCoCrFe high-entropy alloy upon dynamic tension : micromechanism and constitutive modeling. Int. J. Plast. 124, 226–246. https://doi.org/10.1016/j.ijplas.2019.08.013.
Zhilyaev, A.P., Langdon, T.G., 2008. Using high-pressure torsion for metal processing : fundamentals and applications. Prog. Mater. Sci. 53, 893–979. https://doi.org/10.1016/j.pmatsci.2008.03.002.